The Astrophysical Journal, 814:111 (12pp), 2015 December 1 doi:10.1088/0004-637X/814/2/111

SPITZER MICROLENS MEASUREMENT OF A MASSIVE REMNANT IN A WELL-SEPARATED BINARY

Y. Shvartzvald[1,32], A. Udalski[2], A. Gould[3], C. Han[4], V. Bozza[5,6], M. Friedmann[7], M. Hundertmark[8]
and
C. Beichman[9], G. Bryden[1], S. Calchi Novati[5,9,10,33], S. Carey[11], M. Fausnaugh[3], B. S. Gaudi[3], C. B. Henderson[1,3,32], T. Kerr[12], R. W. Pogge[3], W. Varricatt[12], B. Wibking[3], J. C. Yee[13,34], W. Zhu[3]
(Spitzer team),
R. Poleski[3], M. Pawlak[2], M. K. Szymański[2], J. Skowron[2], P. Mróz[2], S. Kozłowski[2], Ł. Wyrzykowski[2], P. Pietrukowicz[2], G. Pietrzyński[2], I. Soszyński[2], K. Ulaczyk[14]
(OGLE group),
J.-Y. Choi[4], H. Park[4], Y. K. Jung[4], I.-G. Shin[4], M. D. Albrow[15], B.-G. Park[16], S.-L. Kim[16], C.-U. Lee[16], S.-M. Cha[16,17], D.-J. Kim[16,17], Y. Lee[16,17]
(KMTNet group),
D. Maoz[7], S. Kaspi[7]
(Wise group),
R. A. Street[18], Y. Tsapras[19], E. Bachelet[18,20], M. Dominik[21,35], D. M. Bramich[20], Keith Horne[21], C. Snodgrass[22], I. A. Steele[23], J. Menzies[24], R. Figuera Jaimes[21,25], J. Wambsganss[19], R. Schmidt[19], A. Cassan[26], C. Ranc[26], S. Mao[27,28,29], Subo Dong[30]
(RoboNet),
and
G. D'Ago[10], G. Scarpetta[5,10], P. Verma[10], U. G. Jørgensen[8], E. Kerins[29], and J. Skottfelt[31]
(MiNDSTEp)
[1] Jet Propulsion Laboratory, California Institute of Technology, 4800 Oak Grove Drive, Pasadena, CA 91109, USA
[2] Warsaw University Observatory, Al. Ujazdowskie 4, 00-478 Warszawa, Poland
[3] Department of Astronomy, Ohio State University, 140 W. 18th Avenue, Columbus, OH 43210, USA
[4] Department of Physics, Chungbuk National University, Cheongju 361-763, Korea
[5] Dipartimento di Fisica "E. R. Caianiello," Università di Salerno, Via Giovanni Paolo II, I-84084 Fisciano (SA), Italy
[6] Istituto Nazionale di Fisica Nucleare, Sezione di Napoli, Italy
[7] School of Physics and Astronomy, Tel-Aviv University, Tel-Aviv 69978, Israel
[8] Niels Bohr Institute & Centre for Star and Planet Formation, University of Copenhagen, Øster Voldgade 5, DK-1350 Copenhagen K, Denmark
[9] NASA Exoplanet Science Institute, MS 100-22, California Institute of Technology, Pasadena, CA 91125, USA
[10] Istituto Internazionale per gli Alti Studi Scientifici (IIASS), Via G. Pellegrino 19, I-84019 Vietri sul Mare (SA), Italy
[11] *Spitzer*, Science Center, MS 220-6, California Institute of Technology, Pasadena, CA, USA
[12] UKIRT, 660 N. Aohoku Place, University Park, Hilo, HI 96720, USA
[13] Harvard-Smithsonian Center for Astrophysics, 60 Garden Street, Cambridge, MA 02138, USA
[14] Department of Physics, University of Warwick, Gibbet Hill Road, Coventry, CV4 7AL, UK
[15] University of Canterbury, Department of Physics and Astronomy, Private Bag 4800, Christchurch 8020, New Zealand
[16] Korea Astronomy and Space Science Institute, Daejon 305-348, Korea
[17] School of Space Research, Kyung Hee University, Yongin 446-701, Korea
[18] Las Cumbres Observatory Global Telescope Network, 6740 Cortona Drive, suite 102, Goleta, CA 93117, USA
[19] Astronomisches Rechen-Institut, Zentrum für Astronomie der Universität Heidelberg (ZAH), D-69120 Heidelberg, Germany
[20] Qatar Environment and Energy Research Institute, Qatar Foundation, P.O. Box 5825, Doha, Qatar
[21] SUPA, School of Physics & Astronomy, University of St. Andrews, North Haugh, St. Andrews KY16 9SS, UK
[22] Planetary and Space Sciences, Department of Physical Sciences, The Open University, Milton Keynes, MK7 6AA, UK
[23] Astrophysics Research Institute, Liverpool John Moores University, Liverpool CH41 1LD, UK
[24] South African Astronomical Observatory, P.O. Box 9, Observatory 7935, South Africa
[25] European Southern Observatory, Karl-Schwarzschild-Str. 2, D-85748 Garching bei München, Germany
[26] Sorbonne Universités, UPMC Univ. Paris 6 et CNRS, UMR 7095, Institut d'Astrophysique de Paris, 98 bis bd Arago, F-75014 Paris, France
[27] Physics Department and Tsinghua Centre for Astrophysics, Tsinghua University, Beijing 100084, China
[28] National Astronomical Observatories, Chinese Academy of Sciences, 20A Datun Road, Chaoyang District, Beijing 100012, China
[29] Jodrell Bank Centre for Astrophysics, School of Physics and Astronomy, University of Manchester, Oxford Road, Manchester M13 9PL, UK
[30] Kavli Institute for Astronomy and Astrophysics, Peking University, Yi He Yuan Road 5, Hai Dian District, Beijing 100871, China
[31] Planetary and Space Sciences, Department of Physical Sciences, The Open University, Milton Keynes, MK7 6AA, UK
Received 2015 August 25; accepted 2015 October 21; published 2015 November 23

ABSTRACT

We report the detection and mass measurement of a binary lens OGLE-2015-BLG-1285La,b, with the more massive component having $M_1 > 1.35\,M_\odot$ (80% probability). A main-sequence star in this mass range is ruled out by limits on blue light, meaning that a primary in this mass range must be a neutron star (NS) or black hole (BH).

[32] NASA Postdoctoral Program Fellow.
[33] Sagan Visiting Fellow.
[34] Sagan Fellow.
[35] Royal Society University Research Fellow.

The system has a projected separation $r_\perp = 6.1 \pm 0.4$ AU and lies in the Galactic bulge. These measurements are based on the "microlens parallax" effect, i.e., comparing the microlensing light curve as seen from *Spitzer*, which lay at 1.25 AU projected from Earth, to the light curves from four ground-based surveys, three in the optical and one in the near-infrared. Future adaptive optics imaging of the companion by 30 m class telescopes will yield a much more accurate measurement of the primary mass. This discovery both opens the path and defines the challenges to detecting and characterizing BHs and NSs in wide binaries, with either dark or luminous companions. In particular, we discuss lessons that can be applied to future *Spitzer* and *Kepler* K2 microlensing parallax observations.

Key words: binaries: general – black hole physics – Galaxy: bulge – gravitational lensing: micro – stars: neutron

1. INTRODUCTION

All known stellar-mass black holes (BHs) are in close binary systems. Presumably this is a selection effect induced by the fact that these BHs have been detected via X-ray emission generated by accretion from a close companion. In the near future, the *Gaia* satellite may detect (or place interesting limits upon) BHs in wider binary systems with main-sequence companions at semimajor axes $0.2 \lesssim a/\mathrm{AU} \lesssim 5$. However, gravitational microlensing appears to be the only way to systematically study the populations of isolated BHs and BHs in well-separated binaries with dark (BH or neutron star (NS)) companions. This is because, in the absence of a luminous companion, BHs do not generate photometric signatures (except possibly when accreting from the interstellar medium), and gravitational lensing is unique in its ability to detect objects based solely on their gravitational field (Einstein 1936).

Gould (2000a) estimated that almost 1% of microlensing events observed toward the Galactic bulge are due to BH lenses, with another 3% due to NS lenses. However, even if this estimate is correct, not a single such lens has yet been definitively identified. The reason is quite straightforward: the principal observable in microlensing events, the Einstein timescale t_E, is a combination of three physical properties of the lens–source system,

$$t_\mathrm{E} = \frac{\theta_\mathrm{E}}{\mu_\mathrm{geo}}; \quad \theta_\mathrm{E}^2 \equiv \kappa M \pi_\mathrm{rel}; \qquad \kappa \equiv \frac{4G}{c^2 \mathrm{AU}} \simeq 8.14 \frac{\mathrm{mas}}{M_\odot}. \tag{1}$$

Here θ_E is the angular Einstein radius, $\pi_\mathrm{rel} = \mathrm{AU}(D_L^{-1} - D_S^{-1})$ is the lens–source relative parallax, and μ_geo is the lens–source relative proper motion in the Earth frame. While the source distance D_S is usually well known, none of the other variables in these equations is routinely measured. Hence, simple parameter counting implies that two other parameters must be measured to determine M and D_L.

Two quantities that can in principle be measured are the angular Einstein radius θ_E and the microlens parallax $\boldsymbol{\pi}_\mathrm{E}$, whose magnitude is $\pi_\mathrm{E} = \pi_\mathrm{rel}/\theta_\mathrm{E}$ and whose direction is that of the lens–source relative motion (see Figure 1 of Gould & Horne 2013 for a didactic discussion). If these two quantities can be measured, then the physical parameters can be disentangled (Gould 1992, 2000b):

$$M = \frac{\theta_\mathrm{E}}{\kappa \pi_\mathrm{E}}; \quad \pi_\mathrm{rel} = \pi_\mathrm{E} \theta_\mathrm{E}; \quad \boldsymbol{\mu}_\mathrm{geo} = \frac{\theta_\mathrm{E}}{t_\mathrm{E}} \frac{\boldsymbol{\pi}_\mathrm{E,geo}}{\pi_\mathrm{E}}. \tag{2}$$

For the great majority of microlensing events, neither π_E nor θ_E is measured. However, for the special case of BH lenses, the Einstein timescales $t_\mathrm{E} = \theta_\mathrm{E}/\mu \propto M^{1/2}$ tend to be long, and this greatly enhances the prospects of measuring π_E via Earth's orbital motion (Smith et al. 2003; Gould 2004). Hence, the main method that has been recognized for identifying BHs and measuring their masses using microlensing has been to attempt to measure θ_E for these long-timescale BH candidates.

However, this same large Einstein radius $\theta_\mathrm{E} \propto M^{1/2}$ diminishes the already tiny chance ($p = \rho = \theta_*/\theta_\mathrm{E}$) that the lens will transit a source of radius θ_*, which is the principal method by which θ_E can be measured for isolated lenses (Gould 1994a; Yoo et al. 2004; Gould & Yee 2013).

More than a decade ago, when microlensing event detections were almost two orders of magnitude less frequent than today, three BH candidates were identified—MACHO-98-6, MACHO-96-5, and MACHO-99-22. Poindexter et al. (2005) subsequently showed that these had, respectively, low, medium, and high probabilities of being BH lenses. However, none was either confirmed or rejected as a BH because there was no measurement of θ_E. The main idea to measure θ_E for isolated BHs is astrometric microlensing, which takes advantage of the fact that the displacement of the image centroid from the true source positions is directly proportional to θ_E (Hog et al. 1995; Miyamoto & Yoshii 1995; Walker 1995). Such measurements are being pursued by several groups although they are challenging with today's facilities. However, they may become routine in the future with *WFIRST* (Gould & Yee 2014).

BHs in relatively wide (~1–10 AU) binaries open a second, less explored path toward BH microlensing mass measurements. In contrast to isolated lenses, binaries often have large caustic structures, which greatly increases the probability that the source will transit these structures. Because the magnification formally diverges to infinity at a caustic, a caustic crossing permits a measurement of $\rho = \theta_*/\theta_\mathrm{E}$, the ratio of the angular source size to the angular Einstein radius, since the observed magnification will be affected by the finite size of the source. Because θ_* is almost always easily measured (Yoo et al. 2004), this yields θ_E. Of course, such measurements require that the events actually be monitored during the typically brief (few hour) caustic crossings, which in the past has required either good luck or very aggressive followup observations. This situation may change with the ramp-up of modern surveys like OGLE-IV and KMTNet, which monitor wide fields at greater than 1/hour cadence for 13 and 16 square degrees, respectively.

To date, however, no such microlensing BH binaries have been discovered. Part of the problem has certainly been missed caustic crossings, but another part is that the entire "paradigm" outlined above actually applies mainly to BHs in the Galactic disk. From Equation (2), the microlens parallax $\pi_\mathrm{E} = \sqrt{\pi_\mathrm{rel}/\kappa M}$. Hence, π_E tends to be small for BHs. If, in addition, the lens is in the Galactic bulge, e.g., $\pi_\mathrm{rel} = 0.01$ mas,

then an $M = 5\,M_\odot$ BH would have $\pi_E = 0.016$. Such small parallaxes are difficult to detect, and especially to measure reliably, from the ground. Moreover, at a proper motion $\mu = 4$ mas yr^{-1} typical of bulge lenses, the timescale would be only $t_E = 60$ days, which is not exceptionally long. Thus Galactic bulge BHs, including BH binaries, are much more difficult to detect and measure from the ground than Galactic disk BHs.

Space-based microlensing parallax is well placed to meet these challenges. Rather than relying on the fairly slowly accelerated motion of a single observer on Earth (Gould 1992), space-based microlensing directly compares contemporaneous light curves from two well-separated observers (Refsdal 1966; Gould 1994b). For an Earth–satellite separation (projected on the sky) $\boldsymbol{D}_\perp$, the microlensing parallax is approximately given by

$$\boldsymbol{\pi}_E = \frac{\mathrm{AU}}{D_\perp}(\Delta\tau, \Delta\beta); \quad \Delta\tau = \frac{t_{0,\oplus} - t_{0,\mathrm{sat}}}{t_E};$$
$$\Delta\beta = \pm u_{0,\oplus} - \pm u_{0,\mathrm{sat}}, \tag{3}$$

where the subscripts indicate parameters as measured from Earth and the satellite. Here, (t_0, u_0, t_E) are the standard point-lens microlensing parameters: time of maximum[36], impact parameter, and timescale. For binary microlensing, these form a subset of a larger parameterization, but the formula remains valid. For point-lens events, precisions at the level $\sigma(\pi_E) < 0.01$ required for bulge-BH mass measurements have been achieved in practice (Calchi Novati et al. 2015). For binaries, the challenge is greater because of an intrinsic asymmetry in the measurement of ($\Delta\tau$, $\Delta\beta$) (Graff & Gould 2002): one linear combination

$$\Delta t_{cc} = (\Delta\tau + \Delta\beta \cot\phi) t_E, \tag{4}$$

can be measured with exquisite precision from the difference in caustic-crossing times Δt_{cc} seen from Earth and the satellite. Here, ϕ is the angle between the source trajectory and the tangent to the caustic. However, the orthogonal combination is much more difficult to measure. We will discuss this challenge in some detail in Sections 3.4, 4–6.

Nevertheless, the main difficulty is the availability of such parallax satellites, which must be in solar orbit (or orbiting a solar system body that is not itself orbiting Earth), capable of reasonably good photometry in the crowded bulge fields, and, of course, allocated to microlensing observations.

Dong et al. (2007) made the first such microlens parallax measurement using the IRAC camera on *Spitzer* for the microlensing event OGLE-2005-SMC-001. This was, in fact, a binary star lens and moreover the favored interpretation was a BH binary. Unfortunately, however, there was no caustic crossing, so this remains a candidate rather than a confirmed detection.

In 2014, the Director allocated 100 hr of *Spitzer* time for Galactic bulge observations with the specific aim of determining *Spitzer*'s viability as a microlensing parallax satellite. Based on this successful test (Calchi Novati et al. 2015; Udalski et al. 2015b; Yee et al. 2015b), which included one mass measurement of a binary (Zhu et al. 2015), 832 hr were awarded for 2015, which is a majority of the 38 days that bulge targets are visible from *Spitzer* due to Sun-angle restrictions.

[36] For binary lenses, this is replaced by time of closest approach to some fiducial point in the lens geometry, which is usually not in fact the maximum.

While the main focus of this program was to determine the Galactic distribution of planets, and the main protocols for both *Spitzer* and supporting ground-based observations were determined on this basis (Yee et al. 2015a), there was also a significant effort to monitor binaries, exactly because of the possibility of mass measurements.

Here we report on the mass and distance measurements of OGLE-2015-BLG-1285La,b. The mass of the primary indicates that it is most likely an NS or a BH. The system lies $<2°$ in projection from the Galactic center and is almost certainly a member of the Galactic bulge population. The field was specifically targeted by OGLE for factor ~5 increased cadence to enable early alerts that would permit timely *Spitzer* observations and to increase the probability of resolving unexpected caustic crossings. It was further targeted as part of a $\sim 4\,\mathrm{deg}^2$ survey by UKIRT and Wise observatories in Hawaii and Israel, respectively, in order to both increase phase coverage and, in the former case, take advantage of the capacity of IR observations to penetrate the relatively high extinction in these fields. The mass measurement of OGLE-2015-BLG-1285 is a specific product of these specially targeted observations.

In Section 2 we discuss the observations, with emphasis on *Spitzer* and the above-mentioned special targeting. In Section 3, we present a microlens model and demonstrate how the physical conclusions follow from the light-curve features and the source position on the color–magnitude diagram (CMD). In Section 4, we show that future proper-motion measurement of the luminous component(s) of the binary lens will yield a decisive mass measurement. In Section 5, we discuss the requirements for breaking similar degeneracies in future events using microlensing data alone. Finally, in Section 6, we discuss some other future prospects.

2. OBSERVATIONS

2.1. Special Northern Bulge Fields

The high extinction toward the Galactic plane in optical surveys roughly splits the Galactic bulge into distinct northern and southern regions. Microlensing surveys traditionally concentrate on southern bulge fields close to the Galactic plane because the event rate there is high and the extinction is relatively low. This maximizes the number of detected events with the high-quality light curves that are required for planet detection. It is of course understood that the northern bulge fields, being roughly symmetric with the south, have just as many microlensing events. However, prior to the 2015 *Spitzer* campaign, only one northern bulge field was targeted for high-cadence observations: OGLE-IV BLG611, centered at $(\ell, b) = (0.33, 2.82)$. Although this field has a long heritage going back almost two decades to OGLE-II, no systematic study had ever been made as to which northern bulge fields were the most profitable to target.

In the course of analyzing the 2014 *Spitzer* campaign, we realized that *Spitzer* target selection was being heavily influenced by optically-based microlensing alerts, whose distribution on the sky was strongly impacted both directly and indirectly by the pattern of dust extinction. That is, first, to the extent that high-extinction fields are surveyed, it is more difficult to find and monitor events because they are systematically fainter in the optical. Second, because of this very fact, these fields tend to be monitored at lower cadence or not at all. By contrast, for any event that can be detected in the optical

(i.e., $A_I \lesssim 4$) *Spitzer* is essentially unaffected by the dust. In 2015, therefore, special efforts were made to counter this bias, which included taking specific account of the extinction at each event location (Yee et al. 2015a). In addition to these general measures, we also identified several northern bulge fields for special observations, including an *H*-band survey using UKIRT (Hawaii) and an *I*-band survey from Wise (Israel). One of the four OGLE fields containing these regions was BLG611, which was already being observed with hourly cadence. But the other three fields—BLG653, BLG654, and BLG675 (cf. Figure 15 in Udalski et al. 2015a)—were raised from cadences of roughly 0.5/day to 2–3/day.

The UKIRT/Wise fields were selected using the procedures developed by Poleski (2015), who showed that the product of the surface densities of $I < 20$ stars and clump stars is a good predictor of the microlensing event rate.

2.2. OGLE Alert and Observations

On 2015 June 7 UT 19:39, the Optical Gravitational Lens Experiment (OGLE) alerted the community to a new microlensing event OGLE-2015-BLG-1285 based on observations with the 1.4 deg^2 camera on its 1.3 m Warsaw Telescope at the Las Campanas Observatory in Chile (Udalski et al. 2015a) using its Early Warning System (EWS) real-time event detection software (Udalski et al. 1994; Udalski 2003). Most observations were in *I*-band, but with some *V*-band observations that are, in general, taken for source characterization. These are not used in the modeling. At equatorial coordinates (17:39:23.75, −27:49:13.0) and Galactic coordinates (0.23, −1.75), this event lies in OGLE field BLG675, with a nominal observing cadence of roughly 2–3 times per night.

2.3. Spitzer *Observations*

OGLE-2015-BLG-1285 originally appeared to be a point-lens event. The protocols and strategies for observing such events with *Spitzer* are reviewed in Street et al. (2015) and are discussed in greater detail by Yee et al. (2015a). In brief, targets were submitted on Monday for observations on the following Thursday through Wednesday for each of the six weeks of the *Spitzer* campaign.

OGLE-2015-BLG-1285 was selected for *Spitzer* observations on Monday June 22 UT 13:33, i.e., for the fourth week of observations, and at standard hourly cadence. Given the time of the OGLE alert, it could not have been selected for the first two weeks. The *Spitzer* team specifically considered this event during preparations for the third week but found its predicted behavior too ambiguous to select it. Even in the fourth week, it was considered highly risky but was chosen specifically because it lay in a field covered by UKIRT and Wise, and so would automatically receive good light-curve coverage. Also, it was noted that the source was probably a red giant and so about 100 times brighter at 3.6 μm than typical targets, even though it was relatively faint in the optical due to high extinction.

In the sixth (final) week, the cadence was increased to 4/day on the grounds that it was apparently anomalous. According to the protocols of Yee et al. (2015a), such increased cadence can be used to characterize the anomaly or increase the precision of the parallax measurement, provided that the anomaly and parallax are detectable without them. Altogether, *Spitzer* observed OGLE-2015-BLG-1285 38 times, with each epoch composed of six 30 s dithered exposures.

2.4. Other Survey Observations

The sky position of OGLE-2015-BLG-1285 was covered by three surveys in addition to OGLE, namely UKIRT, Wise, and KMTNet. As with OGLE, the UKIRT and KMTNet observations were carried out without consideration of any known microlensing events in the field. The Wise observation procedures are discussed explicitly below.

UKIRT observations were carried out with the wide-field NIR camera WFCAM, at the UKIRT telescope on Mauna Kea, Hawaii. WFCAM uses four Rockwell Hawaii-II HgCdTe detectors. The field of view of each detector is $13\farcm6 \times 13\farcm6$ and the four arrays are separated by gaps whose areas are 94% of one detector. The observations were in *H*-band, with each epoch composed of sixteen 5 s co-added dithered exposures (2 co-adds, 2 jitter points, and 2×2 microsteps). The 18 survey fields were observed five times per night.

The Wise group used the recently installed Jay Baum Rich 0.71 m Telescope (C28) at Wise Observatory in Israel, equipped with a 1 deg^2 camera. The four survey fields were observed five times per night. At the time, the C28 had some pointing problems, and OGLE-2015-BLG-1285 was close to the edge of the survey field. Hence, at the initiative of M.F., the Wise group decided to also monitor the event with the Wise 1 m telescope equipped with the PI camera. Because these observations were triggered solely to ensure coverage of an event that was in the survey field, with a cadence similar to that of the survey, we treat these as "survey" observations even though they were taken with a different telescope. In fact, only the PI observations usefully constrain the model, so we do not include the C28 data.

KMTNet is a new survey that employs 4 deg^2 cameras at three sites: CTIO/Chile, SAAO/South Africa, and SSO/Australia (S.-L. Kim et al. 2015, in preparation). While the primary goal of this survey is near-continuous observation of 16 deg^2 in the southern bulge, it supported the *Spitzer* campaign by obtaining data on another 40 deg^2, with cadence of 1–2/day at each telescope. These lower-cadence fields included the location of OGLE-2015-BLG-1285.

2.5. Followup Observations

Sustained followup observations were carried out by the RoboNet team using five telescopes from the Las Cumbres Observatory Global Telescope (LCOGT) in Chile, South Africa, and Australia, and by the Microlensing Follow Up Network (μFUN) 1.3 m SMARTS telescope at CTIO. By chance, these observations did not cover the crucial bump in the light curve, while their coverage of the wings adds only modestly to the survey coverage. Hence, they do not significantly influence the fits. They are nevertheless included for completeness.

The *Spitzer* team issued an anomaly alert for OGLE-2015-BLG-1285 on July 6 UT 14:43 (JD 7210.11) based on a single OGLE data point that was posted on its web page. The Salerno University 0.35 m telescope responded to this alert when the event rose over Italy just five hours later. These data begin at the tail end of the caustic crossing. They qualitatively confirm the exit feature traced by the Wise 1 m. However, we do not include them in the fit because the target brightness was at the margin of obtaining reliable data.

Thus, the results reported here depend overwhelmingly on survey data.

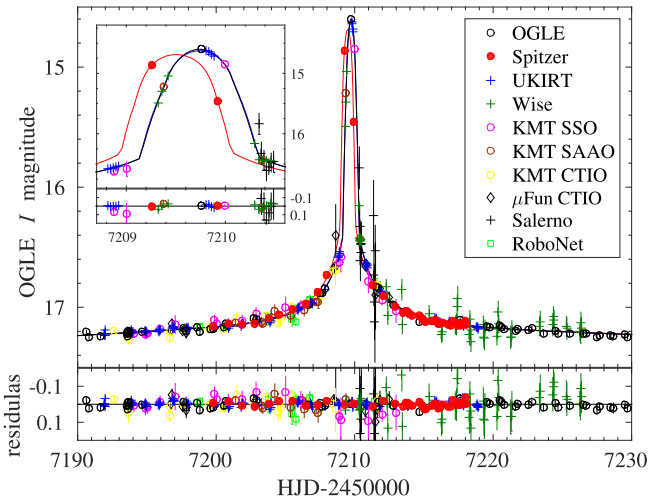

Figure 1. Light curve of OGLE-2015-BLG-1285 with data from *Spitzer* (red) and various ground-based observatories (see interior figure labels). The magnitude scale is what is directly observed by OGLE. All other observatories (including *Spitzer*) are aligned so that equal "magnitude" reflects equal magnification. The very small (∼0.3 day) offset between the peak as seen by *Spitzer* and the ground hints that the microlens parallax $\pi_{\rm E} = \sqrt{\pi_{\rm rel}/\kappa M}$ may be small, which would imply a high-mass lens. For ground-based data, two models are shown, one for *H*-band limb darkening (blue), which should be compared to UKIRT data, and one for *I*-band (black), which should be compared to all other data. The difference between those two curves can be seen only at the peak of the anomaly.

2.6. Data Reduction

All ground-based data were reduced using standard algorithms. Most data entering the main analysis used variants of image subtraction (Alard & Lupton 1998). CTIO-SMARTS, UKIRT, and Wise data were reduced using DoPhot (Schechter et al. 1993), while the LCOGT data were processed using DanDIA (Bramich 2008).

Spitzer data were reduced using a new algorithm (Calchi Novati 2015), the need for which is discussed in Yee et al. (2015a).

3. LIGHT-CURVE ANALYSIS

3.1. Ground-based Light Curve

The light curve contains only a single pronounced feature, which occurs near the peak of a roughly symmetric and otherwise low-amplitude single-lens event, i.e., less than one magnitude above baseline just before and after the sudden anomaly. See Figure 1. In order to properly estimate the masses and projected separation of the components, as well as the distance to the system, we must unambiguously characterize the binary geometry from this single feature, combined with the more subtle variations of the rest of the light curve. From the fact that the *Spitzer* and ground-based light curves are offset by only

$$\Delta t_{\rm peak} \equiv t_{\rm peak,\oplus} - t_{\rm peak,sat} \sim 0.3\ {\rm day}, \qquad (5)$$

(compared to the several-week duration of the event) we already know that the microlens parallax effects can be ignored to first order for the ground-based light curve. However, this still leaves seven geometric parameters to be determined (t_0, u_0, $t_{\rm E}$, t_*, α, s, q). Here, (t_0, u_0, $t_{\rm E}$) are the three parameters of the underlying single-lens event Paczyński (1986), (α, s, q) are the three binary-lens parameters, and $t_* \equiv \rho t_{\rm E}$ is the source crossing time, where $\rho \equiv \theta_*/\theta_{\rm E}$ is ratio of the angular source size to the angular Einstein radius. The three underlying point-lens parameters are, respectively, the time of closest approach to some fiducial point in the geometry, the impact parameter (normalized to $\theta_{\rm E}$), and the Einstein timescale. The three binary parameters are, respectively, the angle of the source trajectory relative to the binary axis, the projected binary separation (normalized to $\theta_{\rm E}$), and the binary mass ratio.

How can we make an exhaustive search of such a large parameter space? We begin by noting that the rough symmetry, dramatic outburst at peak, and lack of significant dip within this peak together imply that the source is moving nearly perpendicular to the binary axis, and that it intercepts a cusp (or two very close and roughly parallel caustics) on this axis. We initially ignore the second, rather special geometry. Then, for each pair (s, q) there are either two cusps (for close and resonant binaries) or four cusps (for wide binaries) on the binary axis. Some cusps can be excluded because perpendicular trajectories would yield pronounced bumps as the source crossed or passed nearby to neighboring cusps. For each of the remaining cusps for a given (s, q), we first set the origin of the coordinate system at the cusp (rather than the center of mass or center of magnification, as is customary). With this parameterization, (t_0, u_0, t_*) are approximately uncorrelated so that at fixed (s, q) there remain only two parameters with significant correlations, $t_{\rm E}$ and α.

We search for solutions using the Monte Carlo Markov chain (MCMC) technique. For each set of trial parameters we employ contour integration (Gould & Gaucherel 1997) for points that either straddle or are very close to a caustic, using 10 annuli to allow for limb darkening. For points that are further from the caustics we progressively use the hexadecapole, quadrupole, and monopole approximations (Gould 2008; Pejcha & Heyrovský 2009). We use linear limb-darkening coefficients of $u_I = 0.61$, $u_H = 0.42$, and $u_{[3.6]} = 0.28$ from Claret (2000), based on the source type derived from Figure 2. In the last case, we must extrapolate. For each model geometry and each observatory, i, we fit for a source flux $f_{s,i}$ and a blend flux $f_{b,i}$ that minimizes the χ^2 of the observed fluxes $F_{i,{\rm obs}}(t)$ relative to the predicted fluxes

$$F_{i,{\rm pre}}(t) = f_{s,i} A(t;\, t_0,\, u_0,\, t_{\rm E},\, t_*,\, \alpha,\, s,\, q) + f_{b,i}\,. \qquad (6)$$

We choose an initial seed trajectory by (t_0, u_0, $t_{\rm E}$, t_*, α) = (7209.75, 0, $t_{\rm E}$, 0.45 day, 90°), where $t_{\rm E} = 30$ day or $t_{\rm E} = 50$ day as discussed immediately below. For the first 100 trials, we allow only u_0 to vary because the crossing may be 0.02–0.1 Einstein radii from the cusp (i.e., $u_0 = 0$), depending on the topology. Then, because (t_0, u_0, t_*) are approximately correct and because there are only two correlated parameters ($t_{\rm E}$, α), the Markov chain arrives near the χ^2 minimum very fast.

There are only two topologies that yield a competitive χ^2. This agrees with the results of two completely independent and generalized search algorithms (VB[37] and CH[38]) that do not make use of the detailed features of the light curve outlined above. In both topologies, the trajectory passes through a cusp of the caustic structure associated with the lower-mass

[37] http://www.fisica.unisa.it/gravitationAstrophysics/RTModel/2015/RTModel.htm
[38] http://astroph.chungbuk.ac.kr/~kmtnet/2015.html

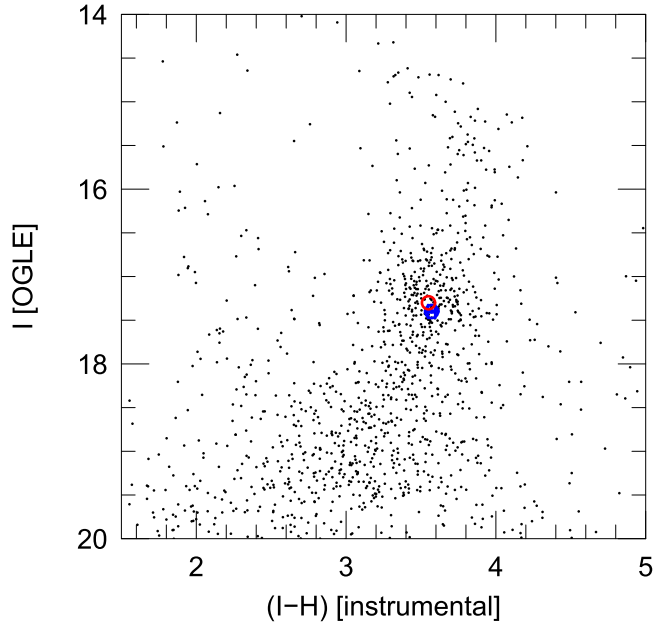

Figure 2. CMD derived by combining calibrated I-band photometry from OGLE with instrumental H-band photometry from UKIRT. The centroid of the clump (red) and the "baseline object" (blue) are marked. From this offset one derives the source radius $\theta_* = 6.01\ \mu\mathrm{as}(f_s/f_{\mathrm{base}})^{1/2}$, where f_s/f_{base} is the ratio of source flux to baseline flux.

component. In the first, it passes by the inner cusp of the lower-mass component, i.e., the cusp that lies closer to the higher-mass component. In the second, it passes by either the outer cusp of this caustic or essentially the same cusp of a resonant binary, i.e., the cusp associated with the lower-mass component. The first topology (see Figure 3 for several examples) typically has timescales $t_{\mathrm{E}} \sim 30$ days, so we use this value in our seeds for this topology. The second topology has $t_{\mathrm{E}} \sim 50$ days, so we seed with this value in those cases. (While the second topology is not shown in Figure 3, it would consist of the source passing roughly perpendicular to the binary axis and right through the bottom-most cusp.)

The "inner cusp" topology is favored by $\Delta\chi^2 = 55$, which is strong evidence in its support. Figure 4 shows $\chi^2(s, q)$ for this topology, and Figure 3 illustrates a range of caustic morphologies drawn from this minimum. In addition to having different topologies, the two solutions are characterized by very different amounts of blend flux. As we will see in the next section, this implies that the inner topology is strongly favored by another, independent argument based on astrometric and chromatic constraints.

3.2. Astrometric and Chromatic Constraints

Neither the position nor the color of the apparent source changes perceptibly as it increases its brightness by a factor ∼15 during the event. This is exactly what one would expect for an unblended source (inner topology) but requires extremely fine tuning for the outer topology[39] ($f_b \simeq 0.68\, f_s$).

[39] We do not discuss this solution in detail because we consider it ruled out. However, for completeness we note that it has (t_{E}, t_*, $\pi_{\mathrm{E},N}$, $\pi_{\mathrm{E},E}$, α, s, q) = (46.3 day, 0.42 day, 0.000, 0.004, 90°.1, 1.56, 7.2) and therefore (M_1, M_2) = (13.7, 1.9) $M_\odot$.

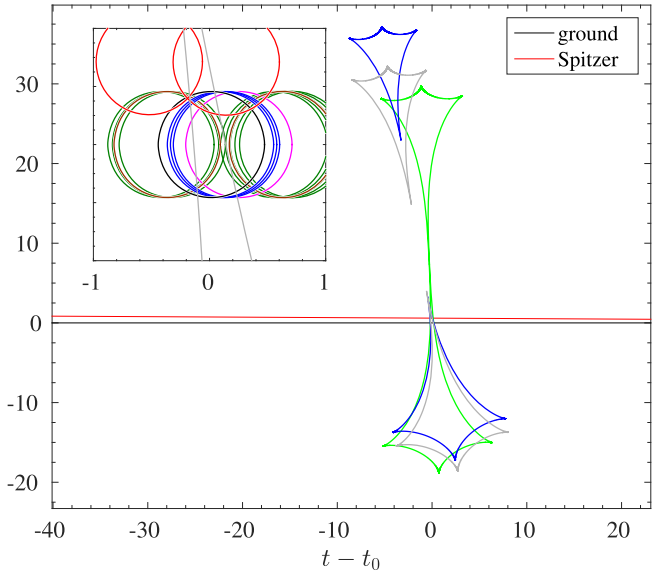

Figure 3. Three different caustic structures that are consistent with the light curve (Figure 1), i.e., from the 2σ region of Figure 4. All three are rotated by α and scaled by t_{E} so that the x-axis is simply source position as a function of time. Hence, the binary axis is oriented so that the primary is toward the top of the plot and the secondary is toward the bottom. Both wide-binary and resonant caustic topologies are permitted. The main panel shows full caustics with *Spitzer* trajectory shown for one of the three caustic structures. Inset is a zoom showing the source size and its position at times of observations, with same color scheme as Figure 1, in which *Spitzer* points are shown relative to the caustic rather than clock time. An alternative topology, which is ruled out by arguments given in Sections 3.1 and 3.2, would have the source trajectory pass through the bottom-most cusp, nearly perpendicular to the binary axis (not shown).

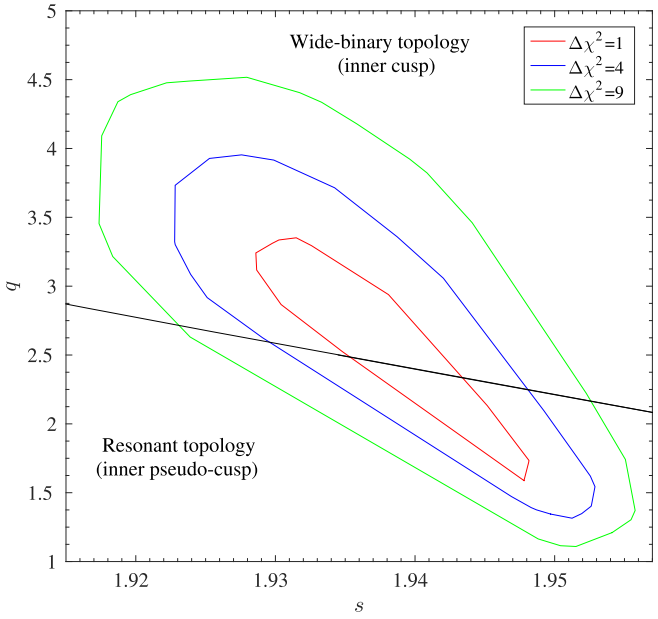

Figure 4. $\chi^2(s, q)$ surface for "inner cusp" topology, where s is the projected separation of the components normalized to θ_{E} and q is the mass ratio of the primary to its companion. The black curve $s^2 = (1 + q^{1/3})^3/(1 + q)$ shows the boundary between wide-binary topology (two four-sided caustics) and resonant topology (one six-sided caustic). See Figure 3.

3.2.1. Chromatic Constraint

Figure 2 is an $(I - H, I)$ CMD constructed by aligning OGLE I-band and UKIRT H-band data. The centroid of the

clump and the "baseline object" at the location of the source are marked. We note that the H-band zero point is not fully calibrated, but such calibration is not needed in the present context because all results are derived from relative photometry.

Model-independent regression of H-band on I-band flux during the event yields

$$\delta(I-H) \equiv (I-H)_s - (I-H)_b \simeq (-0.009 \pm 0.008) \times 10^{0.4(I_b - I_{\rm base})}. \quad (7)$$

Regardless of the degree of blending, the source color is the same as that of the baseline object shown in Figure 2, whose position relative to the clump is

$$\Delta[(I-H), I] = [(I-H), I]_{\rm base} - [(I-H), I]_{\rm clump} = (0.02, 0.10). \quad (8)$$

Since $(I-H)_s - (I-H)_{\rm base} \simeq 0$ to high precision, this permits us to derive

$$\theta_* = 6.01\ \mu{\rm as} \sqrt{\frac{f_s}{f_{\rm base}}}, \quad (9)$$

using the standard method of offset from the clump (Yoo et al. 2004). That is, for a star at the center of the bulge clump $((V-I), I)_{s,0} = (1.06, 14.46)$ (Bensby et al. 2013; Nataf et al. 2013), the source size (if unblended) would be $\theta_* = 6.17\ \mu$as (Bessell & Brett 1988; Kervella et al. 2004). Since the baseline object is fainter by 0.1 mag, this number is reduced by $10^{-0.2\times0.1}$. And since it is redder by $\Delta(I-H) = 0.02$, its surface brightness is lower by 4% (Boyajian et al. 2014), so 2% bigger at fixed magnitude. Hence, $\theta_* = 6.01\ \mu$as, which can then be scaled to the source flux as in Equation (9).

3.2.2. Astrometric Constraint

The source position is measured from the difference image of the event at peak magnification relative to baseline. Since there are no stars except the source in such a difference image, the offset can be measured with great precision, $\sigma = 0.02$ OGLE pixels (each 260 mas). The baseline position is measured from a stack of excellent images and has a precision $\sigma = 0.045$ pixels. Hence, the combined uncertainty in the difference between the positions of the source and the baseline object is $\sigma = 0.05$ pixels or 13 mas. The actual difference in positions is 0.05 pixels in each direction. This is consistent at the 1σ level with the hypothesis of an unblended source.

3.2.3. Application to Outer Cusp Topology Solutions

However, for the outer cusp solution ($f_b \simeq 0.68 f_s$), these constraints together imply that by chance another red giant of very similar color to the source and less than 1 mag below the clump lies within a few tens of mas of the source. There are only four ways that this can happen. Either the blend is directly associated with the source (i.e., they form a red-giant binary), directly associated with the lens (red-giant companion to the binary lens), a component of the lens, or the additional red giant is an unassociated star that lies projected within 40 mas of the source.

The prior probability for the first option (red-giant binary source) can be evaluated in two steps. First, the fraction of G dwarfs (the progenitors of bulge clump stars) with companions within $0.9 < M_{\rm comp}/M_{\rm prim} < 1.0$ is about 3% (Duquennoy & Mayor 1991). On the other hand, for a 10 Gyr solar-mass solar-metallicity isochrone, the mass difference between 25 and 250 solar luminosities (encompassing a conservatively large range of the giant branch) is $M(250\,L_\odot) - M(25\,L_\odot) = 1.8\times10^{-3} M_\odot$. Hence, the prior probability is $0.03 \times (1.8\times10^{-3}/0.1) \sim 5\times10^{-4}$.

The prior probability of the second option (red-giant companion to the binary lens) is somewhat smaller than this, since the conditional probability for a tertiary given a few-AU binary is smaller than the probability of a companion given the presence of a single star.

The prior probability of the third option depends on the details of the solution. However, it is a maximum if the companion mass is of order one solar mass. In this case, the above calculation can be applied but without the binarity factor, i.e., 1.8%. Again, this assumes that the solution predicts $M_1 \sim 1\,M_\odot$ or $M_2 \sim 1\,M_\odot$. Otherwise, the probability is close to zero.

The probability of chance projection is even smaller. First, if the source is separated from the centroid by <40 mas (2σ limit), then it is separated from the blend by <100 mas (assuming roughly equal brightness). In this field, the density of stars that are no more than 1 mag below the clump and within $|\Delta(I-H)| < 0.05$ of a given color (in this case, the source color) is 16 arcmin^{-2}. Therefore the probability of such a projection is $\pi(100\ {\rm mas})^2 \times 16\ {\rm arcmin}^{-2} \sim 10^{-4}$. In sum, the total probability is about 2% for the case that one of the components is about $1\,M_\odot$ and <0.1% otherwise.

3.2.4. Application to Putative Blue Lenses

One may also apply the color constraint to the inner-cusp solutions, for which the blending is constrained by the fit to be small, but may not be exactly zero. In particular, having one or both components be main-sequence stars would in itself be consistent with upper limits on the blended flux. However, the color constraint implies that any such stars must be quite faint. For example, consider F-type stars, e.g., $(I-H)_0 \sim 0.4$. Then $\Delta(I-H) \sim 0.7$, which implies $I_b - I_s \gtrsim 3.5$ at 3σ confidence. This essentially rules out $M > 1.35\,M_\odot$ main-sequence stars.

3.3. Ground-only Microlens Parameters

Figure 4 shows the $\chi^2(s, q)$ surface for the "inner topology." The black curve shows the boundary between wide-binary and resonant caustic topologies (Erdl & Schneider 1993),

$$s^2 = \frac{\left(1 + q^{1/3}\right)^3}{1+q}. \quad (10)$$

That is, while the minimum does lie in the wide-binary caustic topology, the 1σ contour crosses the boundary into resonant caustics. Of course, they cannot cross very far because then the "neck" connecting the two formerly separate wide-binary caustics would widen, leading to a dip in the middle of the bump, which is not seen in Figure 1. Hence, it has proved unnecessary to make an independent search of this narrow-neck resonant topology, mentioned at the beginning of Section 3, since it is contiguous with the inner cusp wide-binary topology.

Table 1 shows the best-fit microlens parameters (including $\pi_{\rm E}$, which is discussed below) and their 68% confidence intervals, derived from the MCMC chain density, leading to

Table 1
Best-fit Microlensing Model Parameters and their 68% Uncertainty Range Derived from the MCMC Chain Density (For Both $u_0 > 0$ and $u_0 < 0$)

Parameter	$u_0 > 0$	$u_0 < 0$
$t_0 - 2457200$ (day)	9.74 [9.73, 9.75]	9.74 [9.73, 9.75]
u_0	0.46 [0.42, 0.53]	−0.46 [−0.42, −0.53]
t_E (day)	31.4 [29.5, 32.5]	31.4 [29.5, 32.5]
$\pi_{E,N}$	0.019 [0.012, 0.029]	−0.018 [−0.012, −0.029]
$\pi_{E,E}$	0.0087 [0.0075, 0.0112]	0.0092 [0.0080, 0.0121]
t_* (day)	0.455 [0.450, 0.459]	0.455 [0.450, 0.459]
q	2.9 [2.1, 3.4]	2.9 [2.1, 3.4]
s	1.934 [1.928, 1.944]	1.934 [1.928, 1.944]
α (deg)	80 [78, 82]	−80 [−78, −82]

Note. We note that there are nonlinear correlations among the parameters, and that the entire χ^2 surface is not parabolic. The solutions are almost symmetric, with a small difference in π_E, due to the small offset between the projected *Spitzer*–Earth axis and the ecliptic.

$\theta_E \sim 0.42$ mas. The χ^2 surface is relatively far from parabolic, and there are nonlinear correlations among the parameters, thus these values should not be considered as standard errors.

3.4. Microlens Parallax from Spitzer Light Curve

The microlens parallax $\boldsymbol{\pi}_E$ of OGLE-2015-BLG-1285 is quite small and can only be measured because of the long baseline $D_\perp \sim 1.25$ AU provided by *Spitzer*. It is straightforward to incorporate *Spitzer* data into the binary-lens fit (e.g., Zhu et al. 2015), add in two parameters for $\boldsymbol{\pi}_E$, and report the result. However, it is also important to gain a physical understanding of how the features of the *Spitzer* light curve act to constrain the parallax.

The strongest constraining feature is the time of peak, which is $\Delta t_{peak} = 0.3$ days earlier than the ground-based peak (Equation (5)). Since the *Spitzer* and ground peaks are both due to the source crossing the binary axis, we find from simple geometry that

$$\frac{\Delta t_{peak}}{t_E} = \Delta\tau + \Delta\beta \cot\alpha. \quad (11)$$

Note that this is identical to the generic Equation (4), but with $\phi \rightarrow \alpha$, which follows from the fact that the caustic is tangent/parallel to the binary axis. Equation (11) can be combined with Equation (3) to yield

$$\pi_{E,\Delta\tau} + \cot\alpha \pi_{E,\Delta\beta} = \frac{\mathrm{AU}}{D_\perp}\frac{\Delta t_{peak}}{t_E} \simeq 0.008, \quad (12)$$

where the subscripts $\Delta\tau$ and $\Delta\beta$ refer to the directions parallel and perpendicular to the projected separation $\boldsymbol{D}_\perp$, which are close to east and north, respectively.

Then, for any given geometry that is consistent with ground-based data, the position of $\boldsymbol{\pi}_E$ within the one-dimensional (1D) space defined by Equation (12) must be determined primarily by the data points on the approach to the cusp. That is, a large value of $\Delta\beta$ would imply that the source crosses the binary axis substantially closer in (or farther out) as seen from *Spitzer* than Earth, leading to a somewhat different cusp-approach morphology. However, because these differences are not expected to be large, and because *Spitzer* observed with only daily cadence, we expect these constraints to be much weaker than those in Equation (11). Hence we expect elongated error contours in the $\boldsymbol{\pi}_E$ plane.

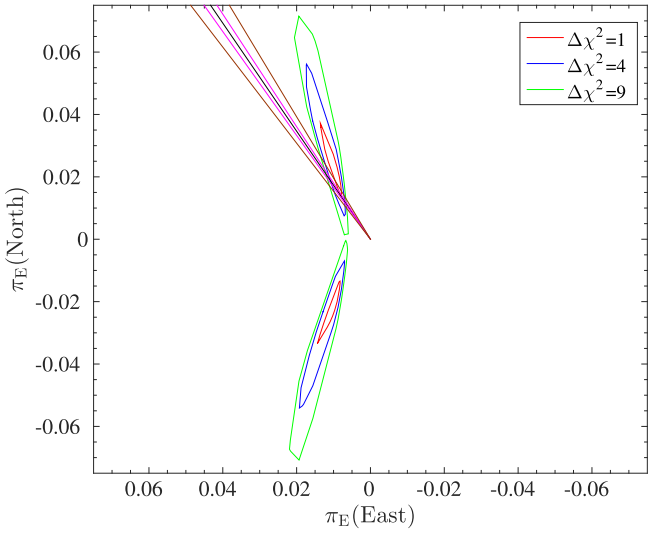

Figure 5. $\chi^2(\boldsymbol{\pi}_E)$ surface. Solutions with $u_0 > 0$ ($u_0 < 0$) lie in the upper (lower) part of the diagram. A physical explanation for quasi-1D contours is given by Equations (11) and (12) in Section 3.4. The magenta and brown rays converging at the origin show the impacts for hypothetical future proper-motion measurements $\hat{\mu} = (60 \pm 1)°$ and $\hat{\mu} = (60 \pm 3)°$, respectively.

Figure 5 shows these contours. For binary lenses with ground-based data there is often a degeneracy that takes $(u_0, \alpha, \pi_{E,N}) \rightarrow -(u_0, \alpha, \pi_{E,N})$ (Skowron et al. 2011), which is sometimes dubbed the "ecliptic degeneracy" because it is exact on the ecliptic. The north component of $\boldsymbol{\pi}_E$ is singled out because the ecliptic happens to run east–west for bulge fields. One expects this degeneracy to be preserved for *Spitzer* because it also lies very close to the ecliptic. Figure 5 shows that this is indeed the case.

Because $M = \theta_E/\kappa\pi_E$, and θ_E varies very little between viable solutions, the total mass M tracks (inversely) the π_E values in Figure 5 very well. However, because a range of mass ratios q are permitted (see Figure 4), the probability contours for the two component masses, M_1 and M_2, (Figure 6) are less 1D than the $\boldsymbol{\pi}_E$ contours. These contours were calculated using the MCMC chain density and accounting for the Jacobian of the transformation between the MCMC variables and the physical quantities as derived in Batista et al. (2011) (see their Equations (17)–(18)). This transformation requires priors on the mass function and the local density of lenses (see definition in Batista et al. 2011). We assume that the mass function is uniform in $\log(M)$, and evaluate from the CMD the bulge distance-modulus dispersion toward the event, $\sigma_{DM} = 0.26$ (Nataf et al. 2013).

Finally, we note that from the definition of θ_E (Equation (1)), and the fact that θ_E is essentially the same in all solutions, we have

$$\pi_{rel} = 10\ \mu\mathrm{as}\left(\frac{\theta_E}{0.41\ \mathrm{mas}}\right)^2\left(\frac{M}{2\ M_\odot}\right)^{-1}. \quad (13)$$

Since the source is nearly at the center of the clump, it is almost certainly in the bulge, with distance $D_S \sim 8$ kpc. Equation (13) then implies $D_S - D_L \simeq 0.6\ \mathrm{kpc}(M/2\ M_\odot)^{-1}$, i.e., that the lens is also in the bulge.

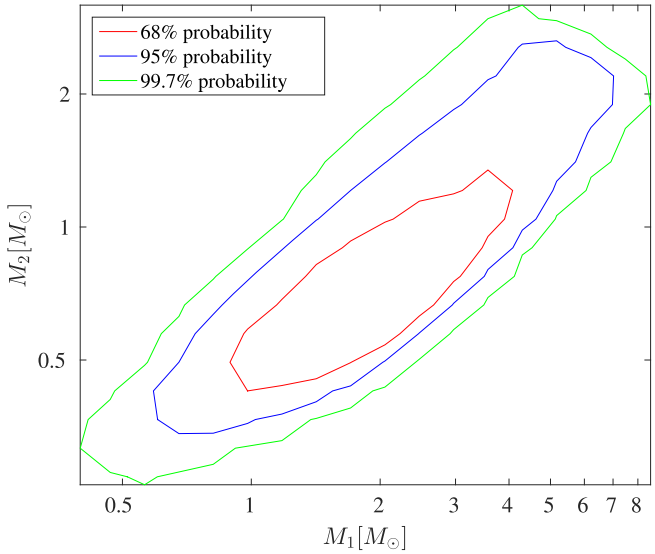

Figure 6. Binary mass map. Contours showing 68%, 95%, and 99.7% probability regions. The most probable combination is an NS primary and a main-sequence secondary. However, binaries with two main-sequence stars or two massive remnants (e.g., BH+NS) are also possible.

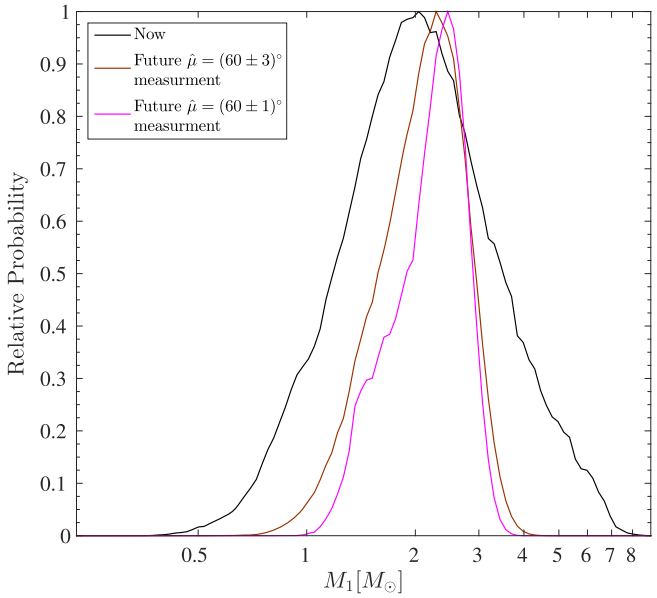

Figure 7. Differential probability distribution of the primary mass M_1, assuming a prior uniform in $\log(M)$, as of "now" (black), i.e., based solely on the microlensing measurement. About 80% of the probability lies above $M_1 > 1.35\,M_\odot$, making this a massive-remnant (NS or BH) candidate. Magenta and brown curves show the impact of future proper-motion measurements $\hat{\mu} = (60 \pm 1)°$ and $\hat{\mu} = (60 \pm 3)°$, respectively, as indicated in Figure 5.

Taking account of the ∼8% error in θ_* (and so θ_E), there is an additional 1σ error in M and π_{rel} of 8% that must be added in quadrature. However, this is smaller than the errors that propagate directly from fitting the light curve.

Figure 7 shows the probability distribution of the primary mass M_1, which is peaked at $M_1 \sim 2.0\,M_\odot$ (black). The fraction of the curve area $M > 1.35\,M_\odot$ (typical NS mass) is 80%. As mentioned in Section 3.2.4, main-sequence stars in this mass range are ruled out by the chromatic constraints. Together, these imply that this primary is a massive-remnant (NS or BH) candidate.

Table 2 summarises the median and the 68% confidence intervals for the physical parameters of the binary system. As for Table 1, we warn about the non-gaussianity and nonlinear correlations among the MCMC variables, which are also reflected in the uncertainties on the physical parameters.

Table 2
Physical Properties of the Binary System

Parameter	Median	68% Confidence Intervals
M_1 ($M_\odot$)	2.0	[1.2, 3.3]
M_2 ($M_\odot$)	0.8	[0.5, 1.2]
$r_\perp$ (AU)	6.1	[5.7, 6.5]
D_L (kpc)	7.5	[7.3, 7.7]

Note. Median and 68% uncertainty range values derived from the MCMC chain density, after accounting for the Jacobian of the transformation between the MCMC variables and the physical quantities.

4. FUTURE MASS DETERMINATION FROM PROPER-MOTION MEASUREMENT

The nature of OGLE-2015-BLG-1285La, i.e., whether it is a massive remnant and if so whether it is a BH or NS, can be decisively resolved by a proper-motion measurement of its companion, OGLE-2015-BLG-1285Lb, whose mass implies that it is almost certainly a luminous low-mass main-sequence star or a white dwarf (see Figure 6). This is illustrated in Figure 5, where we show a hypothetical future measurement of the direction of lens–source relative proper motion $\boldsymbol{\mu}$ with an error of either 3° or 1°. Because π_{rel} is very small, $\boldsymbol{\mu} = \Delta\boldsymbol{\theta}/\Delta t$, where $\Delta\boldsymbol{\theta}$ is the observed lens–source separation at a future epoch $t_{peak} + \Delta t$.

In order to make such a measurement, it is of course necessary for the source and lens to separate. Since their proper motion is known $\mu = \theta_E/t_E \simeq 4.8$ mas yr^{-1}, the wait time depends primarily on the resolution of the telescope. Batista et al. (2015) were able to resolve the source and lens of OGLE-2005-BLG-169 using Keck when they were separated by only 61 mas. However, in that case the source and lens had comparable brightness, whereas here they have a flux ratio $f_l/f_s \lesssim 1\%$. Therefore, it is likely that 15 years would be required with present instruments. However, during this interval, it is likely that 30 m class telescopes with adaptive optics capability will come on-line. By the time that they do, this measurement will already be quite feasible. For example, for separations of $\Delta\theta \sim 50$ mas and limiting resolution FWHM ∼ 11 mas (e.g., in J-band on the Giant Magellan Telescope), a 1° measurement would require that the companion be centroided to 8% of the FWHM in the transverse direction. Improvements to higher precision would be considerably more difficult because the orbital motion of the secondary about the center of mass is of order 0.5 mas.

Figure 7 shows the impact of such a proper-motion measurement on the estimate of the primary mass for ±3° (brown) and ±1° (magenta) errors, respectively. Such a measurement would automatically detect (or rule out) light from a main-sequence (or giant-branch) primary. If the primary is indeed dark, then the detection of light from the secondary would yield a mass estimate of that body, which would in principle constrain the solution and so further constrain the mass of the primary. However, in practice we find that this does

not lead to significant further improvement beyond what can be achieved with the proper-motion measurement alone.

Finally, we note that Gould (2014) has investigated the problem of turning 1D parallax measurements into 2D parallaxes via such proper-motion measurements and shown that, in general, there is a discrete degeneracy induced by the difference between the geocentric frame of the π_E measurement and the heliocentric frame of the μ measurement. While the physical origins of the 1D degeneracy are completely different in the present case, the mathematics, leading to a quadratic equation, are identical. However, in the language of that paper, $A \ll 1$ and $C \ll 1$, so the "alternate" solution (Equation (10) of Gould 2014) is so large as to be easily ruled out by the light curve. Hence, there is no degeneracy.

5. THE GENERAL PROBLEM OF BREAKING THE 1D BINARY-LENS PARALLAX DEGENERACY

As discussed in Section 1, events that have only a single caustic crossing that is monitored from both Earth and a satellite generically suffer from a 1D degeneracy in π_E. See Equations (4) and (11). Breaking this degeneracy, in particular breaking it at the high precision required for bulge-BH mass measurements (with their very small π_E), requires additional high-precision information. In Section 4 we showed that for the specific case of OGLE-2015-BLG-1285, it will be possible to break this degeneracy with future proper-motion measurements, although this still will not deliver a precise mass measurement. Moreover, first, this requires waiting many years, and second it will only be possible because the secondary (or possibly primary) is luminous. Hence, this method will not be applicable to binaries composed of two remnants, which is the unique province of microlensing (and arguably the most interesting case).

Thus, it is of interest to understand how this degeneracy can be broken from microlensing data alone, and in particular, what can be done to modify current experimental protocols to increase the chances of success. Generically, this requires an additional feature in the light curve that is monitored from both Earth and the satellite and whose appearance from the satellite is predicted to be a function of the Earth–satellite separation vector projected onto the Einstein ring. For example, while OGLE-2014-BLG-1050 does suffer from a 1D degeneracy (Figure 3(a) of Zhu et al. 2015), it is much less severe than that of OGLE-2015-BLG-1285. This is primarily because the source trajectory skirts the interior edge of the caustic (Figure 2(a) of Zhu et al. 2015), which has significant structure. Another widespread feature of binary light curves that could provide such leverage is a cusp-approach "bump," which often occurs shortly after a caustic exit.

However, by far the best structure would be a second caustic crossing. In general, if there is a caustic entrance, there must be a caustic exit. This was not actually true of OGLE-2015-BLG-1285 because the source was much bigger than the separation between the caustics, so the entrance and exit combined to form a single bump. However, if the source had been a main-sequence star, i.e., 10 times smaller, there would have been a dip between the the entrance and exit, whose duration would probe π_E in the orthogonal direction (although not with our data set, which has only two *Spitzer* points over the entire cusp crossing).

More generally, however, if there are two independent crossings with measured $\Delta t_{1,2}$ and well-determined crossing angles $\phi_{1,2}$ (derived from the model), then one easily finds

$$\sigma(\Delta\tau) = \frac{\sqrt{\cot^2\phi_1 + \cot^2\phi_2}}{|\cot\phi_1 - \cot\phi_2|}\,\frac{\sigma(\Delta t)}{t_E};$$
$$\sigma(\Delta\beta) = \frac{\sqrt{2}}{|\cot\phi_1 - \cot\phi_2|}\,\frac{\sigma(\Delta t)}{t_E}, \quad (14)$$

where we have assumed that the errors $\sigma(\Delta t_{1,2})$ in the determinations of $\Delta t_{1,2}$ are the same. The most challenging case is clearly $|\Delta\phi| \equiv |\phi_1 - \phi_2| \ll 1$, for which

$$\sigma(\Delta\tau) \to \frac{\sin(2\phi)}{\sqrt{2}\,|\Delta\phi|}\,\frac{\sigma(\Delta t)}{t_E};$$
$$\sigma(\Delta\beta) \to \frac{1-\cos(2\phi)}{\sqrt{2}\,|\Delta\phi|}\,\frac{\sigma(\Delta t)}{t_E}. \quad (15)$$

It is quite plausible to reach errors of $\sim$0.01 days for these time offsets, so that even assuming that the first factors in Equations (14) and (15) are of order $\sim$10, the errors $\sigma(\Delta\tau)$ and $\sigma(\Delta\beta)$ would be only $\sim$0.002 for a $t_E \sim 50$ day event. Thus, coverage of two independent caustic crossings is by far the best method to measure π_E for binaries. We discuss how this can be achieved in practice in the next section.

6. DISCUSSION

While it is not yet known whether OGLE-2015-BLG-1285La,b contains a massive remnant, its example at least shows that such detections are possible. The main challenge to detecting more of these systems is simply to monitor a large number of targets, including not only light curves that already have clear binary signatures but also those (like OGLE-2015-BLG-1285) that erupt with these signatures unexpectedly. *Spitzer* has the advantage that any known microlensing event from the $\sim$100 deg^2 that are currently monitored can be targeted. In contrast to other classes of interesting microlensing events, most particularly free-floating planets, events containing massive remnants tend to be quite long, so that neither the low survey cadence in the majority of these fields nor the relatively long time required to upload targets presents a serious obstacle. A favorable feature of these binaries relative to other microlensing binaries is that, due to their typically small microlens parallax $\pi_E = \sqrt{\pi_{rel}/\kappa M}$, if the binary is seen to be in a caustic trough from Earth, it is likely to also be in the trough as seen from *Spitzer*. Hence, it is likely that at least one of the sharp features induced by caustic crossings will be monitored. However, as discussed in Section 5, such events will generally not lead to a precise mass measurement unless there are additional features in the light curve, such as a post-caustic-exit bump due to a cusp approach. This implies that systems that are monitored from before the caustic entrance, and therefore not usually known to be binaries (e.g., OGLE-2015-BLG-1285) will be the most favorable for precise mass measurements.

Such measurements for these systems would greatly benefit from more aggressive observations from both the ground and *Spitzer*. In the present case, we were fortunate that the microlensed source was a clump giant, with roughly 10 times larger radius than the Sun. This meant that the caustic features lasted 10 times longer than for a solar-type source. Given the relatively sparse coverage over the peak, it is possible that

critical portions of these features would have been missed entirely from the ground if the source had been similar to the Sun. The *Spitzer* observations were even sparser, with only two over the bump. There are a number of modifications that could be made to more than double the cadence of *Spitzer* observations (given the same overall time allocation). In particular, with new real-time reductions (Calchi Novati 2015), it should be possible to stop observations of many events whose *Spitzer* light curve has essentially reached baseline. In addition, it is probably more productive to increase overall cadences at the expense of the 2015 campaign's extra observations for events that are of relatively high magnification as seen from the ground.

For OGLE-2015-BLG-1285, surveys were almost entirely responsible for capturing the peak of the event from the ground (see Section 2). In this respect, two surveys that were specifically created for the *Spitzer* campaign (UKIRT and Wise northern bulge surveys), as well as the wide-area low-cadence survey undertaken by KMTNet in support of this program, played an important role. The continuation of such surveys and the organization of new ones will be crucial. In particular, we note that the VISTA telescope is well placed to do such a survey in highly extincted bulge regions.

However, it is also the case that followup observations could greatly enhance the chances of detecting caustic features in areas that are not well covered by surveys. The primary motivation for such followup observations to date has been planet detection. This both drives the allocation of available followup resources, which are focused on planet sensitivity and detection, and also fundamentally limits the total amount of followup resources to those available to planet hunters. For example, the very intensive LCOGT *Spitzer* support campaign ran out of allocated observing time (due to "too much" good weather!) two days before the peak of OGLE-2015-BLG-1285. While the LCOGT team did arrange to get some additional points of this event in response to the anomaly alert, the main point here is that detection and characterization of BHs is very challenging and observational resources have been limited partly because the potential to detect BHs is not widely appreciated.

The K2 microlensing campaign, scheduled for 83 days beginning 2016 April, will provide a unique opportunity for space-based microlensing without the need for ground-based alerts, and hence with a greater chance that caustic entrances will be monitored from space. This advantage (relative to *Spitzer*) is balanced by the fact that these events will be drawn from a relatively small area, albeit one with close to a peak surface density of microlensing events. From the standpoint of making binary-lens mass measurements, and BH-binary mass measurements in particular, we note that it is exceptionally important that this entire area be monitored from the ground at high cadence and as continuously as possible. For example, even extremely faint stars can give rise to briefly bright caustic crossings that can be effectively monitored by *Kepler* with its 30 minute cadence, even if the majority of the light curve cannot. However, only if the corresponding caustic crossings are monitored from the ground well enough to effectively model the light curve, will this result in accurate mass measurements. A very aggressive attitude toward continuous coverage will be especially important toward the beginning of the campaign when individual southern sites can observe the bulge for only five hours per night.

Gaia will provide complementary information on BH binaries. There are $\sim 3 \times 10^5$ G dwarfs within 250 pc of the Sun, and it is hoped that these will all have $\sigma(\pi) \sim 7\ \mu$as parallaxes by the end of the five-year mission. For any of those that has a BH companion with a period less than the mission lifetime, the semimajor axis of its orbit about the binary center of mass could be measured with the same precision. This would imply 7σ detections for all those in the semimajor axis range $0.015\ \mathrm{AU} < a < 5.3\ \mathrm{AU}$ (assuming $M_{\rm BH} = 5\,M_\odot$). Even the 1.5 year data release would enable detection of those in the range $0.027\ \mathrm{AU} < a < 2.4\ \mathrm{AU}$.

Of course, *Gaia* cannot detect systems that, like OGLE-2015-BLG-1285L, lie in the Galactic bulge, nor can it detect totally dark systems to which microlensing is sensitive. However, *WFIRST* will enable two different probes of BHs that explore both of these regimes. First, it will be able to find and measure the mass of isolated BHs, as well as BH binaries, by combining microlens parallax measurements from its superb photometry with astrometric microlensing from its excellent astrometry (Gould & Yee 2014). For discussion on possible astrometric microlensing measurments with *Gaia* see Belokurov & Evans (2002). Second, it will obtain $\sigma(\pi) < 4\ \mu$as astrometry on about 4×10^7 stars in its microlensing fields (Gould et al. 2015). The majority of these stars will be in the Galactic bulge, where this precision corresponds to a 7σ threshold of $\sim$0.25 AU. Hence, *WFIRST* will be sensitive to BH companions to $\sim 4 \times 10^7$ luminous stars over the range $0.3\ \mathrm{AU} < a < 5.3\ \mathrm{AU}$.

Work by Y.S. was supported by an appointment to the NASA Postdoctoral Program at the Jet Propulsion Laboratory, administered by Oak Ridge Associated Universities through a contract with NASA. The OGLE project has received funding from the National Science Centre, Poland, grant MAESTRO 2014/14/A/ST9/00121 to AU. Work by J.C.Y., A.G., and S.C. was supported by JPL grant 1500811. Work by J.C.Y. was performed under contract with the California Institute of Technology (Caltech)/Jet Propulsion Laboratory (JPL) funded by NASA through the Sagan Fellowship Program executed by the NASA Exoplanet Science Institute. Work by C.H. was supported by Creative Research Initiative Program (2009-0081561) of National Research Foundation of Korea. This research has made the telescopes of KMTNet operated by the Korea Astronomy and Space Science Institute (KASI). L.W. acknowledges support from the Polish NCN Harmonia grant No. 2012/06/M/ST9/00172. D.M. and A.G. acknowledge support by a grant from the US Israel Binational Science Foundation. Work by D.M. is supported by the I-CORE program of the Israel Science Foundation and the Planning and Budgeting Committee. This publication was made possible by NPRP grant # X-019-1-006 from the Qatar National Research Fund (a member of Qatar Foundation) S.D. is supported by "the Strategic Priority Research Program—The Emergence of Cosmological Structures" of the Chinese Academy of Sciences (grant No. XDB09000000). Work by S.M. has been supported by the Strategic Priority Research Program "The Emergence of Cosmological Structures" of the Chinese Academy of Sciences Grant No. XDB09000000, and by the National Natural Science Foundation of China (NSFC) under grant numbers 11333003 and 11390372. M.P.G.H. acknowledges support from the Villum Foundation. Based on data collected by MiNDSTEp with the Danish 1.54 m telescope at the ESO La Silla

observatory. This work is based in part on observations made with the *Spitzer* Space Telescope, which is operated by the Jet Propulsion Laboratory, California Institute of Technology under a contract with NASA. The United Kingdom Infrared Telescope (UKIRT) is supported by NASA and operated under an agreement among the University of Hawaii, the University of Arizona, and Lockheed Martin Advanced Technology Center; operations are enabled through the cooperation of the Joint Astronomy Centre of the Science and Technology Facilities Council of the U.K. This work makes use of observations from the LCOGT network, which includes three SUPAscopes owned by the University of St Andrews. The RoboNet programme is an LCOGT Key Project using time allocations from the University of St Andrews, LCOGT, and the University of Heidelberg together with time on the Liverpool Telescope through the Science and Technology Facilities Council (STFC), UK. This research has made use of the LCOGT Archive, which is operated by the California Institute of Technology, under contract with the Las Cumbres Observatory. The *Spitzer* Team thanks Christopher S. Kochanek for graciously trading us his allocated observing time on the CTIO 1.3 m during the *Spitzer* campaign.

REFERENCES

Alard, C., & Lupton, R. H. 1998, ApJ, 503, 325
Batista, V., Beaulieu, J.-P., Bennett, D. P., et al. 2015, ApJ, 808, 170
Batista, V., Gould, A., Dieters, S., et al. 2011, A&A, 529, A102
Belokurov, V. A., & Evans, N. W. 2002, MNRAS, 331, 649
Bensby, T., Yee, J. C., Feltzing, S., et al. 2013, A&A, 549A, 147
Bessell, M. S., & Brett, J. M. 1988, PASP, 100, 1134
Boyajian, T. S., van Belle, G., & von Braun, K. 2014, AJ, 147, 47
Bramich, D. M. 2008, MNRAS, 386, L77
Calchi Novati, S., Gould, A., Udalski, A., et al. 2015, ApJ, 804, 20
Calchi Novati, S., Gould, A., Yee, J. C., et al. 2015, ApJ, in press (arXiv:1509.00037)
Claret, A. 2000, A&A, 363, 1081
Dong, S., Udalski, A., Gould, A., et al. 2007, ApJ, 664, 862
Duquennoy, A., & Mayor, M. 1991, A&A, 248, 485
Einstein, A. 1936, Sci, 84, 506
Erdl, H., & Schneider, P. 1993, A&A, 268, 453
Gould, A. 1992, ApJ, 392, 442
Gould, A. 1994a, ApJ, 421, L71
Gould, A. 1994b, ApJ, 421, L75
Gould, A. 2000a, ApJ, 535, 928
Gould, A. 2000b, ApJ, 542, 785
Gould, A. 2004, ApJ, 606, 319
Gould, A. 2008, ApJ, 681, 1593
Gould, A. 2014, JKAS, 47, 215
Gould, A., & Gaucherel, C. 1997, ApJ, 477, 580
Gould, A., & Horne, K. 2013, ApJ, 779, 28
Gould, A., Huber, D., Penny, M., & Stello, D. 2015, JKAS, 48, 93
Gould, A., & Yee, J. C. 2013, ApJ, 764, 107
Gould, A., & Yee, J. C. 2014, ApJ, 784, 64
Graff, D. S., & Gould, A. 2002, ApJ, 580, 253
Hog, E., Novikov, I. D., & Polanarev, A. G. 1995, A&A, 294, 287
Kervella, P., Thévenin, F., Di Folco, E., & Ségransan, D. 2004, A&A, 426, 297
Miyamoto, M., & Yoshii, Y. 1995, AJ, 110, 1427
Nataf, D. M., Gould, A., Fouqué, P., et al. 2013, ApJ, 769, 88
Paczyński, B. 1986, ApJ, 304, 1
Pejcha, O., & Heyrovský, D. 2009, ApJ, 690, 1772
Poindexter, S., Afonso, C., Bennett, D. P., et al. 2005, ApJ, 633, 914
Poleski, R. 2015, MNRAS, in press (arXiv:1505.07104)
Refsdal, S. 1966, MNRAS, 134, 315
Schechter, P. L., Mateo, M., & Saha, A. 1993, PASP, 105, 1342
Skowron, J., Udalski, A., Gould, A., et al. 2011, ApJ, 738, 87
Smith, M., Mao, S., & Paczyński, B. 2003, MNRAS, 339, 925
Street, R. A., Udalski, A., Calchi Novati, S., et al. 2015, ApJ, submitted (arXiv:1508.07027)
Udalski, A. 2003, AcA, 53, 291
Udalski, A., Szymanski, M., Kaluzny, J., et al. 1994, AcA, 44, 317
Udalski, A., Szymański, M. K., & Szymański, G. 2015a, AcA, 65, 1
Udalski, A., Yee, J. C., Gould, A., et al. 2015b, ApJ, 799, 237
Walker, M. A. 1995, ApJ, 453, 37
Yee, J. C., Gould, A., Beichman, C., et al. 2015a, ApJ, 810, 155
Yee, J. C., Udalski, A., Calchi Novati, S., et al. 2015b, ApJ, 802, 76
Yoo, J., DePoy, D. L., Gal-Yam, A., et al. 2004, ApJ, 603, 139
Zhu, W., Udalski, A., Gould, A., et al. 2015, ApJ, 805, 8